HOKKAIDO UNIVERSITY

Title	Star formation and ISM morphology in tidally induced spiral structures
Author(s)	Pettitt, Alex R.; Tasker, Elizabeth J.; Wadsley, James W. et al.
Citation	Monthly Notices of the Royal Astronomical Society, 468(4), 4189-4204 https://doi.org/10.1093/mnras/stx736
Issue Date	2017-03
Doc URL	https://hdl.handle.net/2115/65217
Rights	This article has been accepted for publication in [Monthly notices of the royal astronomical society] ©: 2017 Authors Published by Oxford University Press on behalf of the Royal Astronomical Society. All rights reserved.
Type	journal article
File Information	stx736.pdf

Hokkaido University Collection of Scholarly and Academic Papers : HUSCAP

Monthly Notices of the ROYAL ASTRONOMICAL SOCIETY

MNRAS **468,** 4189–4204 (2017)
Advance Access publication 2017 March 24

doi:10.1093/mnras/stx736

Star formation and ISM morphology in tidally induced spiral structures

Alex R. Pettitt,[1★] Elizabeth J. Tasker,[1,2] James W. Wadsley,[3] Ben W. Keller[3] and Samantha M. Benincasa[3]

[1]*Department of Physics, Faculty of Science, Hokkaido University, Sapporo 060-0810, Japan*
[2]*Institute of Space and Astronomical Science, Japan Aerospace Exploration Agency, Yoshinodai 3-1-1, Sagamihara, Kanagawa 252-5210, Japan*
[3]*Department of Physics and Astronomy, McMaster University, L8S 4M1 Hamilton, Canada*

Accepted 2017 March 22. Received 2017 March 18; in original form 2017 February 12

ABSTRACT

Tidal encounters are believed to be one of the key drivers of galactic spiral structure in the Universe. Such spirals are expected to produce different morphological and kinematic features compared to density wave and dynamic spiral arms. In this work, we present high-resolution simulations of a tidal encounter of a small mass companion with a disc galaxy. Included are the effects of gas cooling and heating, star formation and stellar feedback. The structure of the perturbed disc differs greatly from the isolated galaxy, showing clear spiral features that act as sites of new star formation, and displaying interarm spurs. The two arms of the galaxy, the bridge and tail, appear to behave differently; with different star formation histories and structure. Specific attention is focused on offsets between gas and stellar spiral features which can be directly compared to observations. We find that some offsets do exist between different media, with gaseous arms appearing mostly on the convex side of the stellar arms, though the exact locations appear highly time dependent. These results further highlight the differences between tidal spirals and other theories of arm structure.

Key words: hydrodynamics – ISM: structure – galaxies: interactions – galaxies: spiral – galaxies: structure.

1 INTRODUCTION

The origin of spiral arms in disc galaxies remains a debated topic despite a great deal of investigation over the past several decades. The density wave picture of spiral arms popularized by the works of Lin & Shu (1964), Kalnajs (1973) and Bertin et al. (1989) still holds as the canonical theory. However, there are many other competing theories that postulate spiral arms behave as dynamical transients (Sellwood & Carlberg 1984; Elmegreen & Thomasson 1993), can be created by bar rotation (Contopoulos & Papayannopoulos 1980; Athanassoula 1992), tidal interactions (Toomre & Toomre 1972; Elmegreen et al. 1991) and rotations of non-axisymmetric dark matter haloes (Dubinski & Chakrabarty 2009; Khoperskov et al. 2012). The emerging paradigm seems to be that there may not be a grand underlying theory for all spirals; and that each theory has its own merits and weaknesses (e.g. Dobbs & Pringle 2010; Baba et al. 2016). It is likely that the theory that applies depends on a number of factors, such as the galaxy's environment, mass model and evolutionary history. See Dobbs & Baba (2014) and Sellwood (2011) for an in-depth and contemporary reviews of spiral structure theories.

Tidal spirals in particular offer a unique test case due to their ability to generate unbarred two-armed spirals with relative ease, as seen in many theoretical works in the literature (Toomre & Toomre 1972; Donner, Engstrom & Sundelius 1991; Salo & Laurikainen 2000; Oh et al. 2008; Struck, Dobbs & Hwang 2011). As a massive companion passes a host disc galaxy, the tidal interaction induces a trailing two-armed spiral in the disc, with a bridge arm formed in the disc side facing the companion, and a tail arm at the opposite side. The progenitors of this interaction could be dwarf galaxies (e.g. Dobbs et al. 2010) or dark matter subhaloes (Chakrabarti et al. 2011), but in general these spirals are predicted to deviate from density wave and dynamic spirals in several ways. Spiral arms in the density wave picture are expected to induce shocks in the gas as it passes through the stellar potential well (Fujimoto 1968; Roberts 1969). Evidence for which can be seen in the observed thin dust lanes in spiral arms, and high-density gas in simulations (e.g. Wada & Koda 2004; Dobbs & Bonnell 2006). Such shocks are believed to be offset from the stellar potential minima. The azimuthal position of these shocks compared to the stellar spiral is dependent on a number of factors such as rotation curve and gas surface density, and result in shocks being both upstream and downstream of the stellar potential (Gittins & Clarke 2004; Shetty & Ostriker 2006; Wada 2008). However, these shocks are based on the classical density wave picture of spiral arms, and evidence from simulations suggests such shocks in

★ E-mail: alex@astro1.sci.hokudai.ac.jp

© 2017 The Authors
Published by Oxford University Press on behalf of the Royal Astronomical Society

dynamic arms are very different, showing little to no offset between gas and stellar arms (Wada, Baba & Saitoh 2011; Grand, Kawata & Cropper 2012; Baba, Morokuma-Matsui & Egusa 2015).

The case of tidal arms is somewhat more confusing, as they tend to behave somewhere between dynamic and density-wave-like structures. Evidence from simulations suggests that they have a radially decaying yet slower than material pattern speed (Struck et al. 2011; Oh, Kim & Lee 2015). As such, studies in the literature tend to be split on whether they have a negligible (Dobbs et al. 2010; Struck et al. 2011) or slight offset between arms of different media (Pettitt, Tasker & Wadsley 2016, hereafter Paper 1). On the observational side; the most compelling evidence for offset features is in M51, which itself is believed to be a tidally perturbed spiral. Studies looking into numerous tracers in M51 see some offsets in the arms, though the response in each arm seems somewhat different (Schinnerer et al. 2013; Egusa et al. 2017). Other galaxies appear to show some offset features, though the picture is hardly consistent (Kendall, Kennicutt & Clarke 2011). Understanding these offsets could be the key to determining the origin of spiral arms in observed galaxies, so determining their nature in a system such as M51 is of great importance. M51 is also seen to have a pattern speed of its spiral arms that decreases with radius in a similar manner as suggested by tidal interaction simulations (Meidt et al. 2008).

The main method of studying the time-varying properties of different spiral models is through numerical simulations. Galactic simulations have become increasingly sophisticated in recent years, with ever more complex stellar feedback (Agertz et al. 2013; Hopkins et al. 2014), modern hydrodynamical routines (Hayward et al. 2014; Few et al. 2016) and near-pc resolutions (Renaud et al. 2013; Fujimoto et al. 2016). Simulations of isolated galaxies with cooling, feedback and star formation are becoming increasingly common in the literature at high resolutions. Studies exist using both simple analytic background potentials (Saitoh et al. 2008; Dobbs, Burkert & Pringle 2011; Tasker, Wadsley & Pudritz 2015) and resolved stellar systems (Wada et al. 2011; Dobbs, Pringle & Burkert 2012; Hopkins, Quataert & Murray 2012; Renaud et al. 2013; Agertz, Romeo & Grisdale 2015; Goldbaum, Krumholz & Forbes 2016). However, simulations with such complex physics at high resolutions are infrequent in the literature of tidal spirals, and simulations of interactions are often focused on merger events (e.g. Saitoh et al. 2009; Hopkins et al. 2013a), though early stages of mergers are often progenitors of spiral arms. Such mergers tend to cause strong boosts in the star formation activity, up to 10 times that of the isolated value, though this is a strong function of model configuration (e.g. Di Matteo et al. 2008; Hopkins et al. 2013a). Gabor et al. (2016) perform simulations of fly-by and mergers with both grid and particle codes. They found that while different numerical methods tend to give similar global results, the Eulerian models gave a smoother gas disc than the Lagrangian runs, though this could be due to differences in the subgrid physics in each code. Di Matteo et al. (2007) performed a huge parameter sweep of simulated interactions and mergers, though with a comparably low resolution. Their interactions show starbursts during interactions, with new star formation mostly due to infall of gas to the galactic centre, and that strong interactions can be effective in subduing star formation activity due to stripping gas from the host galaxy. Recently, Moreno et al. (2015) investigate the spatial distribution of star formation events in an interaction/merger scenario, finding that star formation is boosted only in the initial companion passage, and will then die away to below pre-interaction levels.

In our previous study on tidal structure (Paper 1), we performed a parameter sweep of simulations looking into the impact of different companion masses, orbits and inclinations on the spiral features formed in a disc galaxy. We found evidence of interarm spurs, variations in structure as a function of interaction strength, and longevity of spiral arm pitch angles and pattern speeds. These models were, however, quite simplistic in nature, only including hydrodynamics and gravity and simulating only the warm neutral medium ($T = 10\,000$ K). In this work, we investigate the fiducial simulation from Paper 1, using a much greater resolution and breadth of physics (including cooling, star formation and stellar feedback) to investigate the nuances of spiral arm features formed in a tidal encounter in a more realistic interstellar medium (ISM) model. Such a study of the locations of star formation, gas morphology and arm structure appear lacking in the literature, with studies instead studying idealized isothermal or *N*-body models, or focusing efforts on modelling mergers and their Gyr scale evolution.

This paper is organized as follows. In Section 2, we discuss the numerical models, including the various physical processes, numerical code and simulation initial conditions. In Section 3, we present our results and discussion. Section 3.1 looks at gas in a static axisymmetric stellar disc potential, which acts as a test case for the ISM models. Section 3.2 presents calculations using a live *N*-body disc before the introduction of the companion, and Section 3.3 the perturbed live galactic disc. We conclude in Section 4.

2 NUMERICAL SIMULATIONS

2.1 Hydrodynamics and gravity

Simulations were performed using the *N*-body+smoothed particle hydrodynamics (SPH) code GASOLINE (Wadsley, Stadel & Quinn 2004), a descendant of the gravity tree-code PKDGRAV (Stadel 2001). Gravity is solved using a binary tree, and the system integrated using a kick-drift-kick leapfrog. Self-gravity is active for all components, using a fixed gravitational softening of 10 pc. We choose to use the standard M4 cubic spline kernel with 64 neighbours.

2.2 Cooling

The gas in these simulations is initially isothermal with a temperature of 10 000 K, and is allowed to cool using a tabulated cooling function from Shen, Wadsley & Stinson (2010), which spans a temperature and density ranges of $1\,\mathrm{K} \leq T \leq 1 \times 10^9\,\mathrm{K}$ and $1 \times 10^{-9}\,\mathrm{cm}^{-3} \leq n \leq 1 \times 10^4\,\mathrm{cm}^{-3}$. Similarly to Benincasa et al. (2016), we use a metal depletion factor of 0.6 to ensure the creation of a two-phase ISM. In addition to metal cooling, we also include UV and photoelectric heating. However, unlike in Benincasa et al. (2016) and Tasker & Tan (2009), who use a radial dependence tailored to the Milky Way, we adopt a constant factor approximately equal to that at the solar radius. This is due to the galaxies being modelled not necessarily as Milky Way analogues, with the tidally perturbed case having disc scalelengths and surface densities that are likely to vary strongly with time.

These values were chosen to give a thermal profile that supposedly mimicked that of the ISM, namely of a two-phase equilibrium (Wolfire et al. 2003). An example of our phase curve is shown in Fig. 1. This figure clearly shows the two-phase medium with populations peaking at around 10 000 and 200 K for the warm and cold neutral media, and reaching temperatures as low as 20 K. While the cooling table goes to lower temperatures, increased resolution and molecular chemistry are needed to model this correctly, thus we enforce a 10 K lower limit in these calculations. A pressure

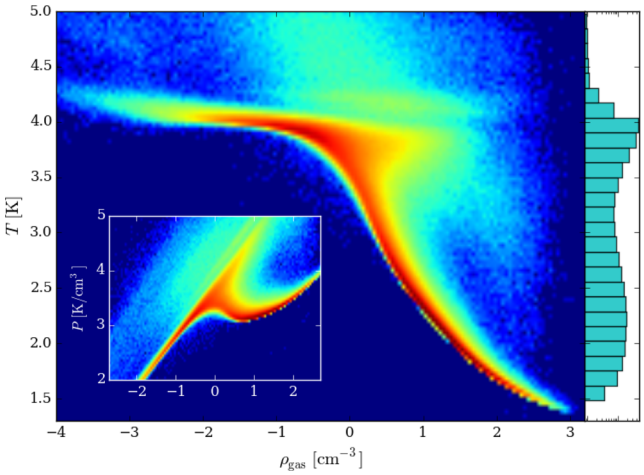

Figure 1. Temperature–pressure–density diagrams for the cooling/heating functions used in this study. The main frame shows a density map of the density–temperature profile of all gas particles, with a histogram of temperature to the right-hand side. The small insert shows the pressure–density profile, clearly showing the two-phase nature of the ISM. The data here are from the static axisymmetric disc calculation after 500 Myr of evolution (see Section 2.5.1).

floor prevents artificial fragmentation below resolution scale, and is calculated as $P_{\rm floor} = 3\rho^2 l^2 G$, where $l = \max(h, \varepsilon_{\rm grav})$ is the spatial resolution (Agertz, Teyssier & Moore 2009) set to the maximum of smoothing lengths (h) and gravitational softening ($\varepsilon_{\rm grav}$).

2.3 Star formation

We use standard subgrid single-stellar-population star formation models (Katz 1992; Katz, Weinberg & Hernquist 1996; Stinson et al. 2006). The main parameters governing star formation are c_*, the star formation efficiency, and $n_{\rm SF,\,min}$, the density threshold. We use a value of $n_{\rm SF,\,min} = 100\,{\rm cm}^{-3}$, $c_* = 6$ per cent, and a maximum temperature for star formation of $T_{\rm SF,\,max} = 300\,{\rm K}$ in all the simulations presented here. Several studies have investigated the impact of changing these parameters, so we simply adopt similar values to other studies at this scale (Tasker & Bryan 2006; Saitoh et al. 2008; Tasker & Bryan 2008). For each star formation event only a single star is created from the parent gas particle, meaning a 100 per cent conversion of a gas particle to a single star particle. This ratio is often chosen to be around a third of the gas particle mass (Okamoto et al. 2005; Governato et al. 2007; Ward et al. 2016) giving a good balance between dynamical complexity and resolution. However, here we choose a 1 : 1 ratio to ensure particle masses are approximately equal, regardless of type, to lessen errors in the SPH method when using unequal particle masses.

2.4 Feedback

Stellar feedback is included from SNII and SNIa supernovae, and winds, in a blast wave feedback approach with a standard cooling shut-off for each gas particle in the blast wave (see Stinson et al. 2006 for details). We adopt a feedback energy of Type II SN, $E_{\rm SN}$ of 10^{50} erg. This gives reasonable star formation rates (SFR) when combined with our value of c_*, which gives a SFR of the order of $1{-}10\,{\rm M}_\odot\,{\rm yr}^{-1}$.

We also experimented with two other feedback schemes, the constant cooling delay feedback of Agertz et al. (2013) and the superbubble feedback of Keller et al. (2014). However, while each proposes improvements over the blastwave model, we found strong ring features in the constant cooling delay runs (see also Benincasa et al. 2016) and muted morphological features in the superbubble runs (see also Keller, Wadsley & Couchman 2015; Mayer et al. 2016). As such we employed the widely adopted blast wave model due to the more responsive morphological features and SFR.

2.5 Simulation parameters

We describe three different simulation models. The Static model where gas is embedded in a static axisymmetric potential, the Live model where an N-body system of particles represents the old stars and halo, and the Pert model where the Live model experiences the tidal interaction of a passing companion.

2.5.1 Static stellar disc

While the main part of this investigation focuses on the tidally perturbed system, we also include a much simpler model to act as a control group. The purpose of this run is to establish a benchmark against the live and perturbed systems (see Sections 2.5.2 and 2.5.3), where the live stellar systems will act to churn and disturb the ISM. This simple model consists of a gas disc embedded in a simple logarithmic potential to represent a Milky Way-like flat rotation curve (Binney & Tremaine 1987) of the form

$$\Phi(r, z) = \frac{1}{2} V_0^2 \log\left[r^2 + R_{\rm c}^2 + z^2/q_z^2\right] \tag{1}$$

where the radial core radius is $R_{\rm c} = 1\,{\rm kpc}$, the vertical scaling factor is $q_z = 0.7$ and flat rotation speed is $V_0 = 220\,{\rm km\,s}^{-1}$. Gas is set radially in an exponential disc with scalelength $r_0 = 7\,{\rm kpc}$ (approximately double the Milky Way's stellar disc), and vertically following a ${\rm sech}^2(z/z_0)$ profile where $z_0 = 0.4\,{\rm kpc}$. The system has a resolution of 4 million gas particles of combined gas mass of $4 \times 10^9\,{\rm M}_\odot$ out to a radius of 10 kpc. Gas is initialized at 10 000 K with a solar metallicity (0.013). This setup is similar to previous works of gas embedded in a galactic potential, such as Saitoh et al. (2008), Dobbs et al. (2011), Tasker et al. (2015) and Benincasa et al. (2016). The system is then allowed to evolve with all physics active from initialization.

2.5.2 Isolated multicomponent system

Here, we use the same mass model as Paper 1 where the gas is set using the MAGALIE initial conditions generator (Boily, Kroupa & Peñarrubia-Garrido 2001). We utilize a much higher resolution version of the model in Paper 1, with a resolution of 3×10^6 gas particles, 3×10^6 old disc stars, 1×10^5 bulge stars and 1×10^6 halo particles. The rotation curve and initialization are identical to Paper 1. This disc to halo mass ratio was chosen so that the system has a high arm number in isolation, and impedes bar formation. The gas disc setup is slightly different from the previous as we utilize an extended gas disc out to 20 kpc; with double the radial scalelength of the gas disc, since gas discs are observed to be flatter and extend further than their stellar counterparts (Tacconi & Young 1986; Binney & Merrifield 1998). We use a gas disc of mass $6 \times 10^9\,{\rm M}_\odot$, which gives a similar surface density to the Static model (Section 2.5.1), that is, of the order of $10\,{\rm M}_\odot\,{\rm pc}^{-2}$.

We allow this live system to relax isothermally for 600 Myr (approximately two rotations) before activating the cooling, star formation and feedback. This allows for the gas disc to relax, and the system to begin forming spiral-like features.

2.5.3 Perturbed multicomponent system

The perturbing computation is the same setup as Paper 1 using a resolved companion composed of 10 000 point mass particles, giving a mass resolution similar to that of the dark matter halo of the host galaxy. The total mass of the companion is $2 \times 10^{10}\,\mathrm{M}_\odot$ and is initialized as a Plummer sphere using MAGALIE (Boily et al. 2001). The companion contains no gas component, and is made of an inert old stellar population (no feedback), but could equivalently be assumed to be a dark matter subhalo. The companion is introduced to the system 200 Myr after the star formation, feedback, and cooling are activated in the multicomponent disc (i.e. 800 Myr after initialization), so that the star formation has reached a pseudo-equilibrium state before the companion is introduced. The companion approaches a near-parabolic orbit in the x–y plane, with an initial position of $y = 40$ kpc and a velocity magnitude of 190 km s^{-1}. This gives a closest approach of approximately 20 kpc from the centre of mass of the host galaxy, and a velocity difference with a magnitude of 275 km s^{-1} (giving an orbital frequency of 14 km s^{-1} kpc^{-1}). The mass ratio of the companion to the host galaxy is 0.092, or equivalently 2/3 of the host stellar disc. These values correspond to a strength parameter for the interaction of $S = 0.1$ (Elmegreen et al. 1991). See Paper 1 for further details regarding the perturbed morphology in a simplified hydrodynamics+gravity only case.

3 RESULTS AND DISCUSSION

3.1 Gas disc in an axisymmetric static potential

The simplest model here is Static model, shown in Fig. 2. The top panels show a top–down gas density render and a vertical profile, and the bottom panel shows a mock stellar image, both after 400 Myr of evolution. The mock stellar image was made using the PYNBODY package (Pontzen et al. 2013) using the metallicity and ages of newly formed stars to calculate luminosities in i-v-u bands mapped to r-g-b colour channels. The disc shows a flocculent spiral in the gas. A power mode analysis of spiral features showed that no spiral mode is dominant (up to $m = 6$) in the stars or the gas. Several cavities are formed by the stellar feedback, slightly increasing in size with increasing disc radius. The stellar image shows weaker axisymmetric structure, with new (bluer) stars showing the clearest asymmetry, and brightness dropping off to the disc edge (as expected form the exponential gas disc).

The star formation history (SFH) for this and the Live calculation (see Section 3.2) are shown in Fig. 3. The SFH shows a clear peak as the gas initially cools and collapses from the initial 10 000 K, which causes this burst in star formation. This then levels off to a normal rate of about 1.5 $\mathrm{M}_\odot$ yr^{-1} for the duration of the simulation. This is similar to what is seen in other disc simulations (Saitoh et al. 2008; Dobbs et al. 2011; Hopkins, Narayanan & Murray 2013b; Benincasa et al. 2016; Grisdale et al. 2017; Rosdahl et al. 2017) and is a result of the initial fragmentation and cooling of the disc. A mild transient ring of old stars seen is visible in the mock stellar image (at a radius of about 8 kpc) that has propagated from the centre. This ring was much clearer in simulations with a greater feedback efficiency, and is likely a result of the initial fragmentation from the idealized isothermal initial conditions.

A measurable characteristic of well-observed disc galaxies is that between gas surface density, Σ_{gas}, and star formation surface density, Σ_{SFR}. This Kennicutt–Schmidt relation (KS relation; Schmidt 1959; Kennicutt 1998) takes the basic form

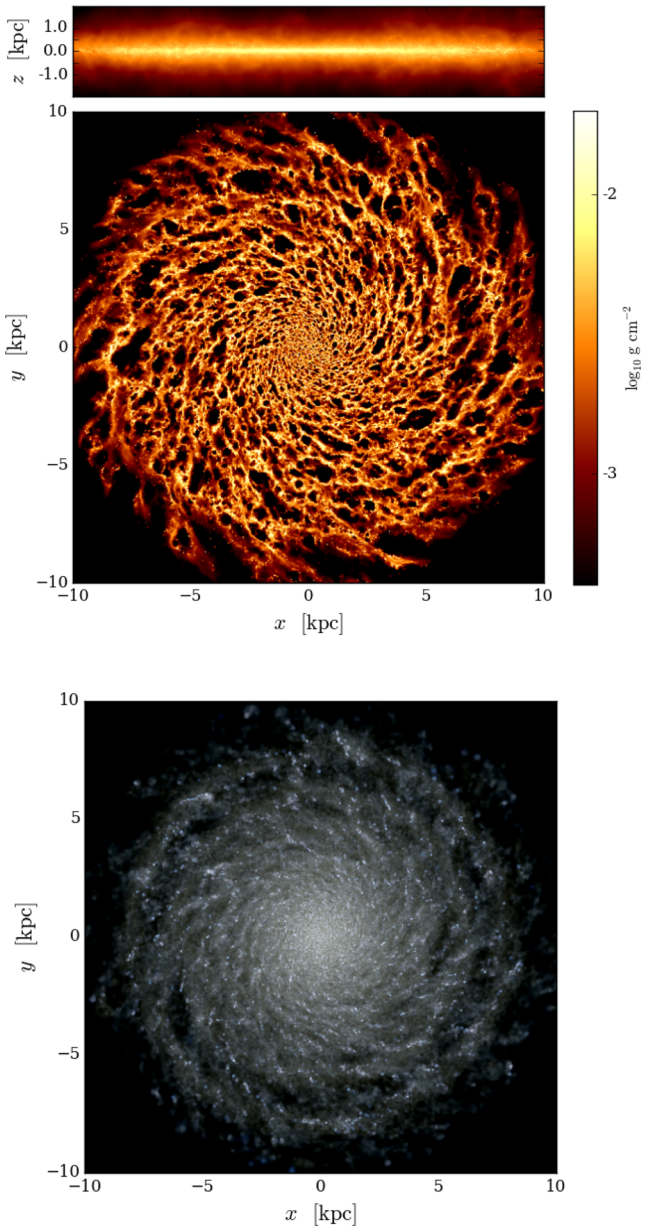

Figure 2. Gas (top) and stellar (bottom) material in Static simulation which includes a static, axisymmetric background potential. The gas is shown as an integrated column density map through the entire domain, while the stellar map shows mock three-colour image of the stars (rbg) dictated by the ages of the stars formed in the simulation. Both images were made using the PYNBODY package (Pontzen et al. 2013).

of

$$\Sigma_{\mathrm{SFR}} = (2.5 \pm 0.7) \times 10^{-4}\,\mathrm{M}_\odot\ \mathrm{yr}^{-1}\ \mathrm{kpc}^{-2} \times \left(\frac{\Sigma_{\mathrm{gas}}}{1\,\mathrm{M}_\odot\ \mathrm{pc}^{-2}}\right)^{1.4\pm0.15} \quad (2)$$

on a galactic scale, whereas smaller scale star formation follows somewhat different relations (Bigiel et al. 2008). We plot this relation for the Static simulation in Fig. 4 as blue circles. We plot equation (2) as a black line with error bounds represented as shaded region, and 10 per cent and 1 per cent of this rate as dashed and dotted lines, respectively. The points for the simulation are calculated at 1 kpc annuli over the entire disc, with the highest surface

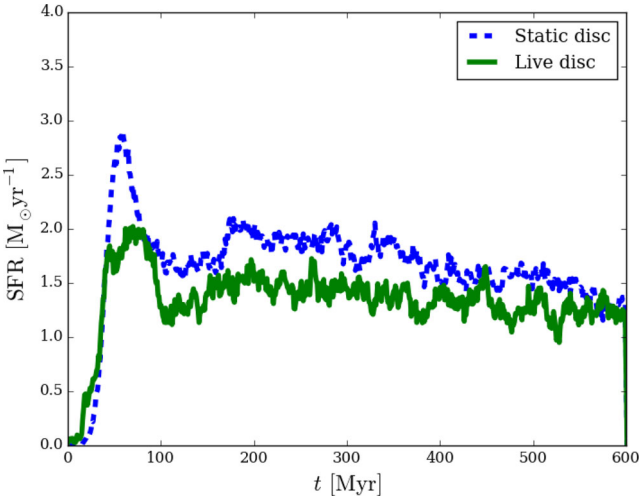

Figure 3. Star formation histories for the Static (blue dashed) and Live (solid green) stellar disc simulations. Rates are calculated across the entire galactic disc.

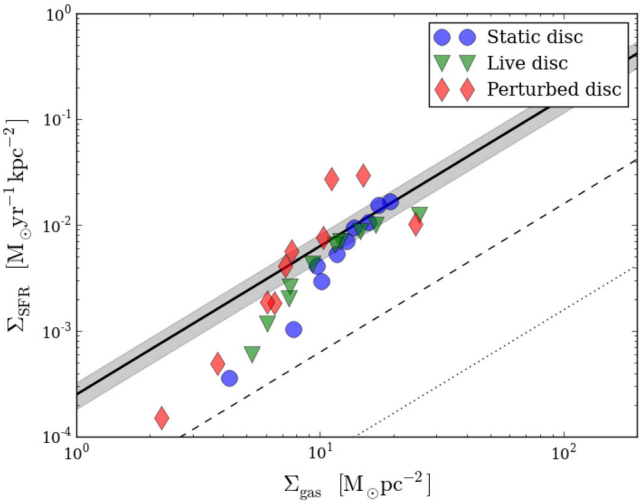

Figure 4. The KS relation for star formation in disc galaxies for the calculations shown here after 600 Myr of evolution with star formation, cooling and feedback active. The shaded grey line shows the observationally motivated KS law with error bounds denoted by the shaded region, with laws of 10 per cent and 1 per cent the fiducial formation efficiencies denoted by the dashed and dotted lines, respectively. Each point denotes a radial annulus bin of width 1 kpc.

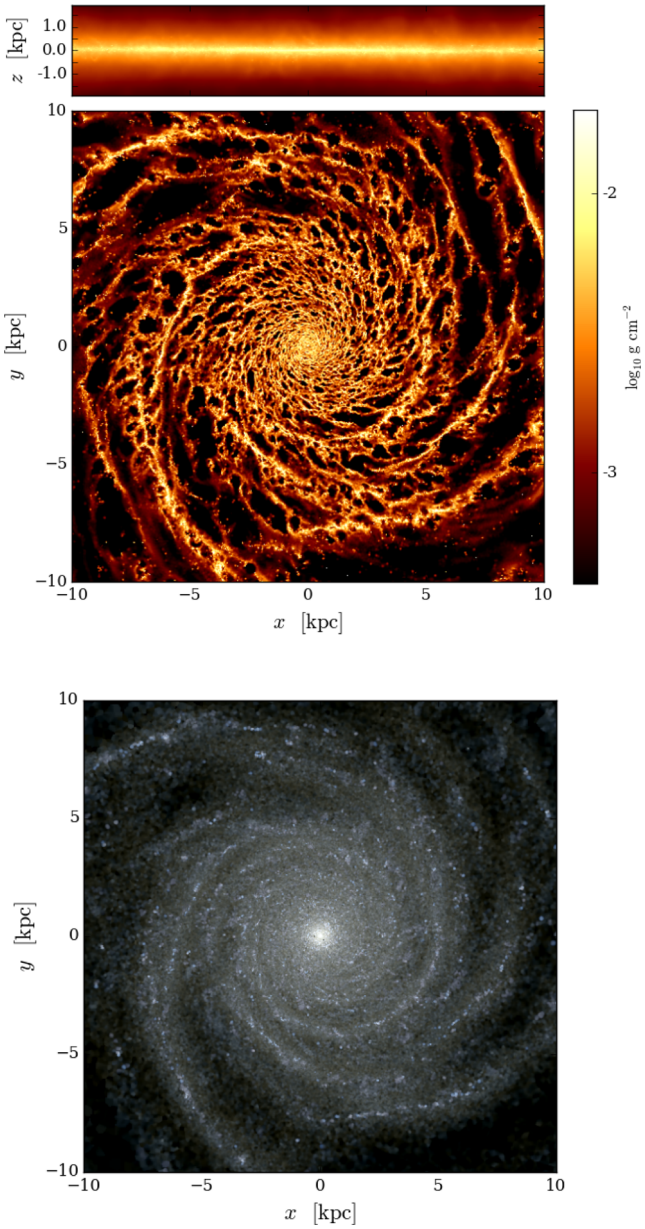

Figure 5. As Fig. 2 but for the live isolated disc. Note that the stellar mock image includes the old stellar population.

density point being the disc centre. The measured points follow the KS relation reasonably well, and tail off at low surface densities similar to the sub-kpc measurements of Bigiel et al. (2008).

The purpose of this model is to act as a control test for the cooling (Fig. 1 uses the data from this model), feedback and star formation on these scales, and many of the multitude of parameters involved were chosen to give sensible phase curves, SFR and morphology.

3.2 Isolated live galactic disc

In Fig. 5, we show a similar plot to Fig. 2, but for the Live calculation after 400 Myr of the activation of cooling, star formation and feedback. In this case, the mock stellar image is made of both old and new stellar components, where the old stars (those present at $t = 0$) have been assigned an age corresponding to the simulation duration and solar metallicity (the old population is responsible for the central bulge emission). The disc has developed a clear multi-armed spiral component in both the gas and the stars. At the time-stamp shown the dominant mode in the mid-disc is $m = 3$, with the dominant arm mode increasing with increasing radius in accordance with swing amplification theory [see other recent simulations: (Pettitt et al. 2015; D'Onghia 2015)]. Once again the gas shows clear cavities caused by clustered stellar feedback, showing a marked difference to the stellar density. High-density gas arms tend to be coincident with the stellar arms, this will be discussed further in Section 3.3.3.

Figs 3 and 4 include the data from this model, shown as the green line and triangle points, respectively. The SFH shows a similar initial burst as the Static calculation, though relatively shallower compared to the equilibrium rate. This calculation has a steadier SFH at late times, maintaining a rate of about 1.3 M$_\odot$ yr^{-1}, whereas the Static

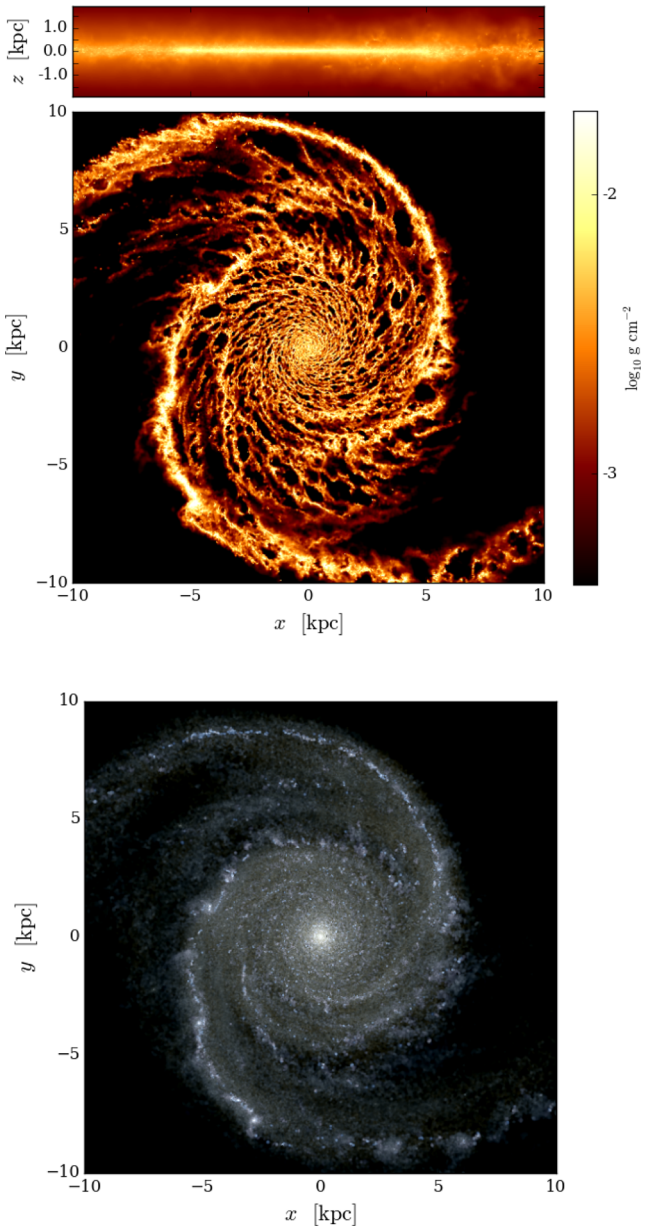

Figure 6. As Fig. 5 but for the perturbed galactic disc, 400 Myr after the inclusion of the companion (approximately 200 Myr after the closest approach).

model shows a gradual decay on the Gyr time-scale. The points in Fig. 4 show only minimal difference to the Static model, though this is on a logarithmic scale compared to the data in Fig. 3. The slightly higher values in the outer disc result from the spiral presence triggering star formation, whereas the Static disc has only gas self-gravity and a much lower mass young stellar disc to seed collapse. The lower value for the central radii is due to the random bulge star orbits stabilizing the disc to collapse, compared to the Static disc where only rotational shear stands in the way of star formation.

3.3 Perturbed live disc

3.3.1 Basic morphology

Fig. 6 shows the stars and gas in the perturbed galactic disc 450 Myr after the introduction of the companion into the system. The central disc is very similar in appearance to the isolated live disc (Fig. 5), and the tidally induced two-armed component dominates outside of approximately 3 kpc. The lack of inner spiral features is the product of the mass model and rotation curve. A massive bulge was chosen to inhibit bar formation, which allows for the study of the tidal spiral without contamination by bar-driven spiral arms. As such the high Q-barrier that suppresses bar formation also inhibits the penetration of the spiral arms to the inner disc. We will be studying the impact of different mass models on the tidal response in a future study (Pettitt et al. in preparation). The mock stellar image shows regions of fresh star formation predominately along the spiral arms, coincident with the high-density gas.

A time-series of the perturbed gas disc is shown in Fig. 7 from the time of closest approach (20 kpc from galactic centre) to 800 Myr after. The white arrows point to the position of the companion, with a length proportional to the distance from the host centre of mass. Directly after closest approach a strong bridge is made between the companion and the host, with the tail formed on the opposite side of the disc. As the disc winds up, the gas experiences a widespread collapse along the spiral arms, which in a few extreme cases causes the creation of large dense knots (e.g. 0.7 and 1.1 Gyr). Once formed, these knots orbit around the disc at the material pattern speed and slowly migrate towards the galactic centre over the course of many rotations. The spiral arms themselves only appear to last for 2–3 disc rotations. After this, they stray from the regular logarithmic-spiral structure, wounding up, as well as disrupted by feedback and clump passage though the arms.

3.3.2 Star formation history

Fig. 8 shows the SFH of the perturbed galactic disc in red over a period of 1.2 Gyr. The vertical dashed line shows the time when the companion is introduced to the simulation, and prior to this the SFH has the same form as the unperturbed live disc in Fig. 3. The dotted vertical line indicates the closest approach of the companion. Note that the peak in star formation at 50 Myr from the initial fragmentation is identical to that in Fig. 3. Closest approach marks the beginning of a steep rise in star formation activity, with the rate reaching a peak of 6 $M_{\odot}$ yr^{-1}, approximately four times that of the unperturbed rate. This peak occurs at 650 Myr, shortly after the 0.6 Gyr density render in Fig. 7. The top–down map suggests that the tail arm is reaching higher densities compared to the bridge arm and interarm disc. This is caused by pile-up/crowding of orbits in the tidal tail, while bridge orbits are disrupted by continued presence of the companion. This will be discussed in detail later in this section, and has been reported in previous works (e.g. Elmegreen et al. 2000; Oh et al. 2008). The near-simultaneous collapse of the gas in the tail arm is the cause of the peak in at 650 Myr in Fig. 8, and two high-density clumps resulting from this collapse can be seen in the interarm regions in the 0.7 Gyr time-stamp in Fig. 7. The next burst in star formation is seen around 750 Myr, which appears to coincide with the collapse of the bridge arm, shortly after the 0.7 Gyr render in Fig. 7. This suggests that the arms have multiple times of collapse, with the tail collapsing before the bridge, and then experiencing another burst event at a later time. The undulating trend then continues throughout the simulation, but progressively weaker with time until the SFR becomes comparable with the unperturbed state.

The companion stripped away gas from the primary during its passage. Fig. 9 shows the companion 800 Myr after the closest approach. A small disc of gas has been accreted on to the quiescent

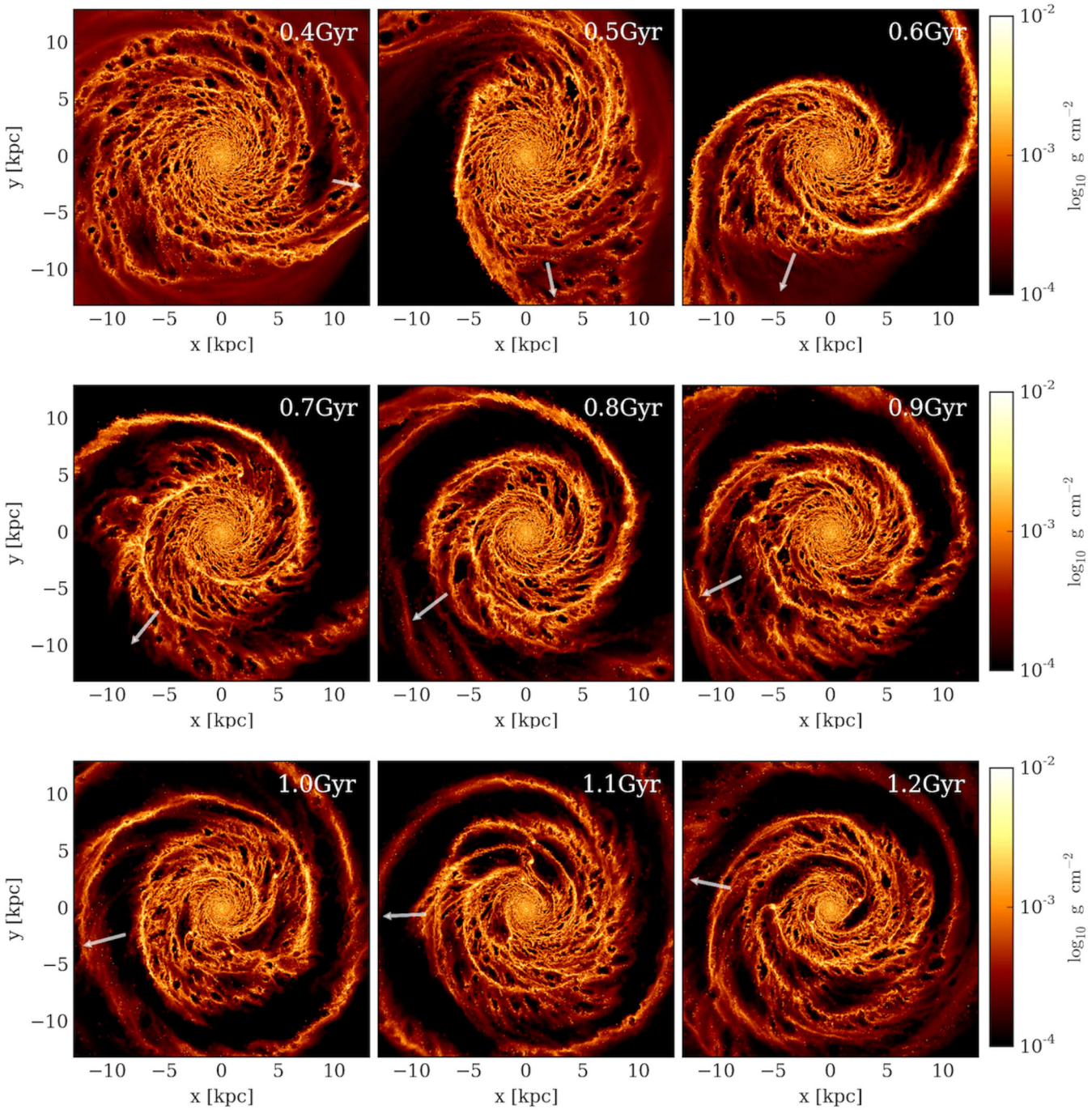

Figure 7. Time series top–down density renders of gas in the perturbed galactic disc for the immediate 800 Myr after the closest approach of the companion. The white arrow points in the direction of the companion, where the length is proportional to the distance away from the main galaxy.

and axisymmetric stellar companion, which then proceeds to form its own new star particles as it moves away from the host system. At the time of Fig. 9, the companion has captured approximately $3.5 \times 10^8\,\mathrm{M}_\odot$ of gas from the host galaxy, though contains $2.5 \times 10^8\,\mathrm{M}_\odot$ of new stars that have formed at least partially from captured gas (as well as $7 \times 10^8\,\mathrm{M}_\odot$ of captured old stars from the host stellar disc). The cyan dashed line in Fig. 8 shows the SFH inside the companion. It shows a clear increase after the closest approach and then settles into a semi-steady state for nearly 600 Myr. The minor increase before the closest approach is due to companion capturing stars that have formed on the outskirts of the host disc and are located within the companion post-interaction. Note, however, that mass transfer to companions is a complex process, and will vary strongly on the impact parameter, galaxy to companion mass ratio and the orbital inclination in both fly-bys (Wallin & Stuart 1992) and collisions (Struck 1997).

We select arm regions from the main disc to further investigate the star formation within each individual arm. In Fig. 10, we show the perturbed disc at four time-stamps where we have highlighted the newly formed stars, defined here as having ages <50 Myr, as

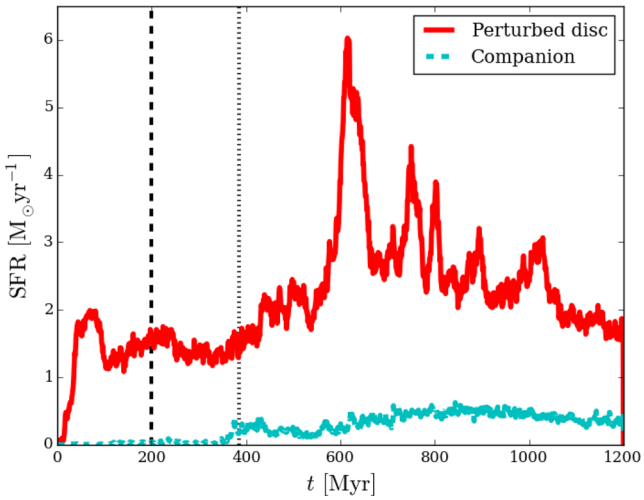

Figure 8. Star formation histories for the perturbed live stellar disc (red solid line) and the companion (cyan dashed line). The vertical dashed line shows the time when the companion is introduced to the system, and the dotted line indicates the time of the closest approach.

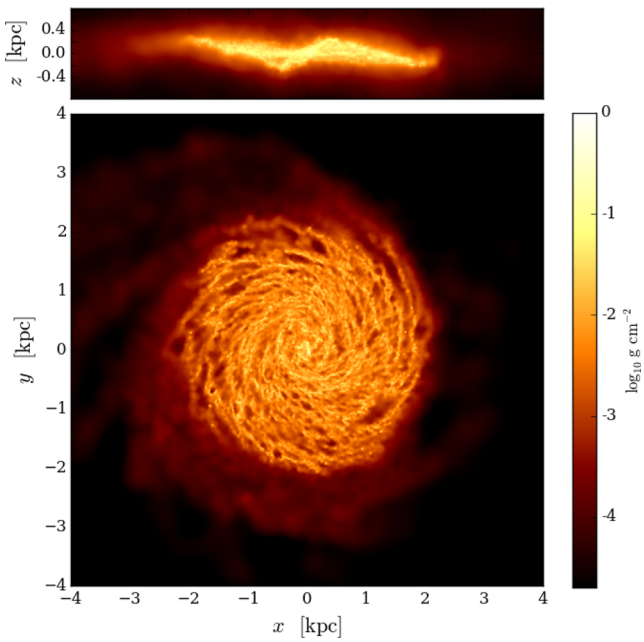

Figure 9. Surface density render and vertical profile of the gas in the companion, 800 Myr after the closest approach with the host galaxy. A flocculent disc has been accreted on to initially gas-free structure.

the coloured points overplotted on a density render of the gas. Blue and red points indicate stars formed within the bridge and tail arms, respectively, and white indicates the interarm young stars. Arms are defined by fitting a two-armed log-spiral to the old stellar disc (see Section 3.3.3 for details), with the arm region encompassing $4\pi/10$ radians. There is still ample star formation in the interarm regions, though the star formation in the arms is heavily clustered and contains approximately 50–90 per cent of the star formation activity, depending on the epoch.

The star formation surface density for each of the arm regions is plotted as in Fig. 11 at the same four different times as in Fig. 10, with matching colour codes for each arm. The total SFR for each arm is given in the bottom-left insert. The $\Sigma_{\rm SFR}$ drops towards

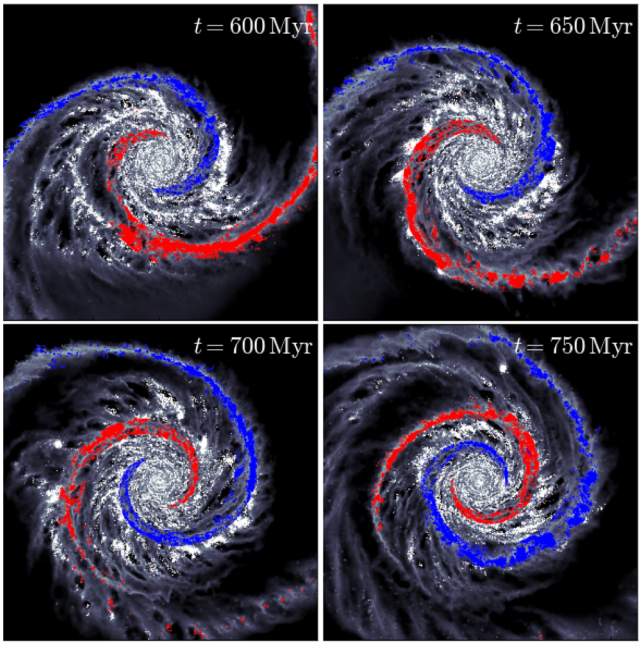

Figure 10. The sites of new star formation in the perturbed disc at four times shortly after companion closest approach. Newly formed stars are coloured red and blue for the tail and bridge arms, respectively, and white for interarm stars in the same age bandpass as those shown for the arms. A density render of the gas is plotted under the stars for reference.

the disc edge, following the gas surface density profile. The trends between the two arms follows what was postulated by inspection of the undulating nature of the global SFR (Fig. 8). The arms appear to swap in terms of star formation efficiency, with the tail arm experiencing the stronger star formation activity at 600 Myr, and the bridge arm showing stronger rates at 750 Myr. The star formation activity also appears to retreat towards the galactic centre over time, owing to the spiral features gradual winding up. This can be seen from the top–down maps of Fig. 10, where we can see the radial extent of new stars being smaller in the 650 Myr map compared to that of 600 Myr (both for arm and interarm regions).

The cause of this offset in collapse times and SFH between the two arms is due to two effects. The first is the nature of the orbits in each arm. In Oh et al. (2008), the authors showed that the tail arm is made of collective overlapping of particle orbits on the far side of the disc (see their fig. 5). Whereas the orbits in the bridge have been elongated in a teardrop-like feature and are experiencing forced oscillations due to the close proximity of the companion. The infalling gas then flows through the density-wave-like bridge feature in a steady stream that extends to the perturber. Also note the much sharper arm–interarm contrast in the tail arm where the orbits of almost all particles have become coincident, compared to the bridge arm which still has a large amount of upstream gas ready to fall in the bridge region and a weaker arm–interarm contrast. Elmegreen et al. (2000) also saw such tidal pile-ups in the tail arms of simulations, and inferred that such mechanisms were occurring in the interacting galaxy IC 2163 (see their fig. 2). Recent observations of this galaxy made using the Atacama Large Millimeter Array also show a strong pile-up of molecular gas into 'eyelid'-shaped arm features that also display asymmetries between bridge and tail regions (Kaufman et al. 2016).

The second reason for this SFH offset is that much of the bridge arm gas mass has transferred to the perturber. In Di Mat-

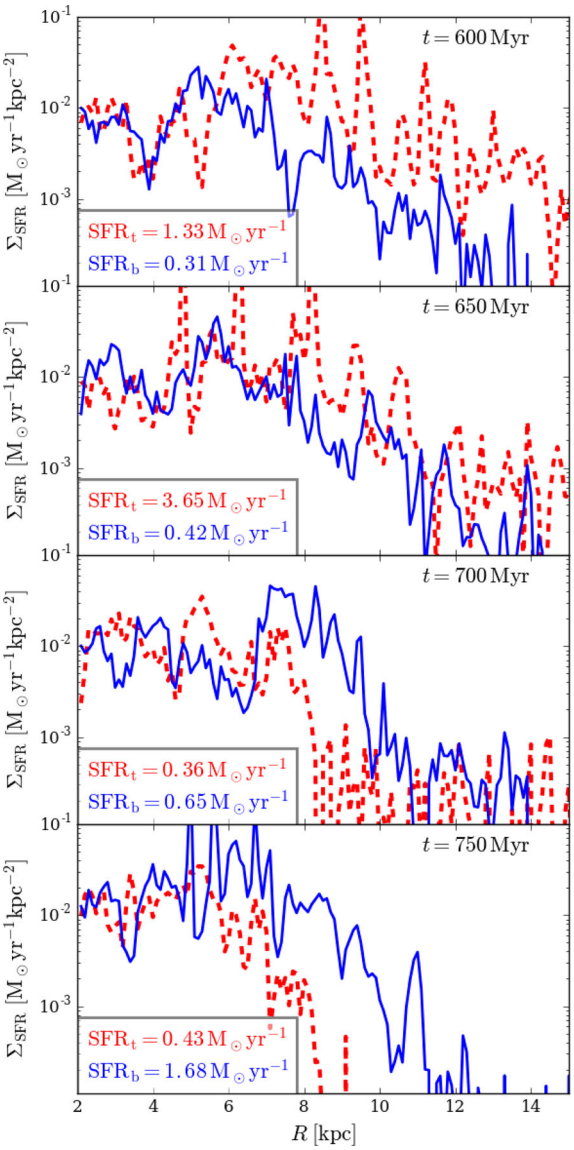

Figure 11. The surface SFR in the arms in each of the time-stamps in Fig. 10. Red and blue lines represent the tail and bridge arms, respectively. The total SFR in each arm is shown in the bottom left of each panel.

teo et al. (2007), strong interactions tended to disrupt and mute star formation on a galactic scale due to stripping of the gas disc by the companion. In our models, the tidal forces are not strong enough to cause widespread stripping, but have instead transferred a significant amount of the gas budget via the bridge tidal arm (seen in Fig. 9). This causes the bridge arm to have a deficit in star-forming gas compared to the tail arm, which would result in the asymmetric SF properties seen in Fig. 11.

3.3.3 Shocks and offsets

We now look at the offset of gas and stellar structures in these simulations. To do so, we fit logarithmic spiral functions to the Live and Pert simulations at multiple time frames, which is a function of the form:

$$\theta = \ln(R/R_o)\cot(\alpha) \quad (3)$$

where the pitch angle is α, and the parameter R_o simply defines the initial azimuthal position of the spiral at $r = 0$. We fit arms using the same method as described in Paper 1, using a combination of Fourier decomposition and a fitting routine to constrain equation (3) to the simulated arms.

In the Live simulation, with feedback and star formation at the same time as Fig. 5, we find the dominant mode to be that of $m = 3$ and pitch angle of $\alpha = 18^\circ$. The exact values tend to fluctuate somewhat with time, but a spiral feature is persistent approximately half a rotation until it is wound up and sheared away. The perturbed stellar disc behaves similarly to Paper 1, in that a strong $m = 2$ spiral starts off very wide and winds up of the order of a few rotations. For the time frame of the perturbed disc shown in the following figures, the pitch angle is approximately $\alpha = 16^\circ$ at 700 Myr and $\alpha = 11^\circ$ at 800 Myr.

In Fig. 12, we show the gaseous (left-hand column) and stellar (right-hand column, encompassing all ages) material from the Stat (top row), Live (second row) and Pert (third and below) simulations. We show three time-stamps of the perturbed simulation as the morphology is highly time dependent. In the fourth row, we show the 700 Myr time-stamp for the Pert simulation without cooling, star formation and feedback (noFBSF). For the Live and Pert models, material has been shifted in azimuth to align with the spiral arm fit of the old stellar population in each simulation, with the vertical black lines signifying the log-spiral arm fit. The Static model has not been shifted due to a lack of prevailing spiral mode, showing a clear flocculent morphology in the these projections in both the stars and the gas. Bins have been then normalized to the azimuthally averaged surface density at each radius to remove the impact of the exponentially radial decay of the material and highlight overdensities. While clearly the old stars do not trace the log-spiral perfectly at all radii, the function provides a good match for the mid-disc in all cases. The Live disc in particular is not entirely axisymmetric of the order of the fitted spiral, and there was also significant power in other modes at this time. The dominant arm number increases with radius in the stellar disc, with an $m = 2$ mode around $R = 3$ kpc, $m = 3$ at $R = 5$ kpc, $m = 4$ at $R = 7.5$ kpc and an $m = 5$ feature approaching $R = 10$ kpc[1]. The Pert disc shows $m = 2$ dominating at all times, at most radii in the disc, with the gas showing large cavities in the interarm regions compared to the Live case. The 600 Myr time-stamp of the Pert simulation shows residual $m = 3$ mode signatures in the mid-disc, the same features as in the unperturbed Live calculation. Note that small spurs/feather-like features can be seen in the Live and Pert gas discs. However, the ones in the Live run are significantly smaller features, and extrude at a shallower angle compared to the spiral arms. The spurs in the Pert disc appear larger and at a near-tangential angle to the spiral arms in some cases. The Pert and Pert-noFBSF runs have very similar morphology, with interarm branches appearing in the same position in both.

We plot the azimuthal position of the particles binned into annuli of 1 kpc width in Fig. 13 for the isolated live disc, and Fig. 14 for the perturbed disc at 700 Myr. Each vertical panel shows different radii, and the black dashed lines are again the fitted spiral arms. The dashed magenta lines show the gas, while the grey and dotted green lines show the old and newly formed stars, respectively (chosen

[1] This is in accordance with predictions of swing amplification theory for axisymmetric perturbations, where the predicted spiral arm number is given by $m \approx \kappa^2 R/4\pi G\Sigma$, where κ is the epicycle frequency (Toomre 1981; Sellwood & Carlberg 1984; Bottema 2003), see Dobbs & Baba (2014) sections 2.1.3 and 2.2.1 for a more contemporary discussion.

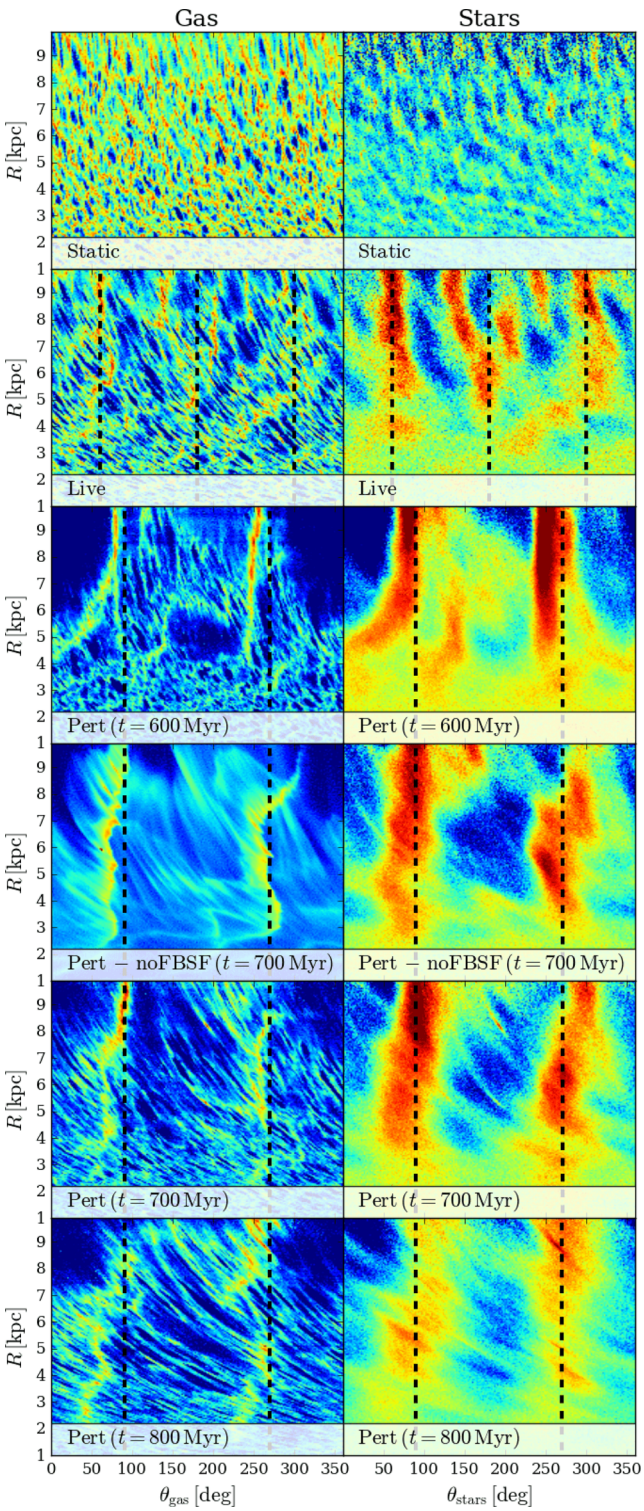

Figure 12. The spiral arms folded into $R - \theta$ space in the Static, Live, Pert and Pert-noFBSF calculations. On the left are the gaseous features, and on the right are the stars. Three time-stamps of the Pert calculation have been included, separated by 100 Myr. For Live and Pert models, material has been aligned with a fit to the stellar spiral arms, with black dashed lines showing the fitted arm minima.

here as $t_{\rm age} \leq 40$ Myr). Note that for the perturbed disc, we have masked out two large clumps in the disc for clarity. These clumps can be clearly seen in Fig. 6, giving clear narrow spikes in the binned distributions, and are dynamically decoupled from the spiral arms. We only plot data in the range 3 kpc $< R <$ 10 kpc, as there are only weak spiral features further inward, and particle density drops considerably further out.

The Live stellar disc simulation shown in Figs 12 and 13 has no strong offset between any of the media, with gas, stellar and young stellar peaks seemingly coinciding at all radii. This is also seen to be the case in other studies of live discs (e.g. Wada et al. 2011; Grand et al. 2012; Baba et al. 2015). The gas and young stars tend to show a greater arm–interarm contrast compared to the old stellar arms. In the inner disc (3–4 kpc), there appears to be some minor offset between the stars and gas, though inspection of Fig. 12 shows the arm features are extremely weak at this radius compared to the mid and outer disc.

The Pert simulation however appears to show some asymmetries between the different disc material. Even by-eye inspection of the particle binning in Fig. 12 is enough to see that there are some positions where the gas and stars have a non-zero offset (e.g. 3 kpc $< R <$ 7 kpc in the 700 Myr time frame). Inspection of Fig. 14 shows the offsets clearly, especially in the outer disc where the induced spiral is stronger. The offset appears to be strongest in the tail arm feature. The young stars tend to behave very similar to the gas, with only a young clump at 7 kpc as the main outlier. As the definition of 'young' stars is made to encompass a wider age range, the young stars tend to trace the same features as the old (i.e. present from $t = 0$ Myr) stellar population, whereas as the range is narrowed they coincide more with the gas arms.

To further hone-in on this offset, we follow an analysis similar to that of Egusa et al. (2017), who analyse the spiral arm offsets in the grand design galaxy M51. In their work, the authors trace spirals in the gas and stars across the disc and measure their azimuthal positions relative to each other. We fit the spiral features using both of their approaches. The first is a simple peak-finding method in the vicinity of the spiral (i.e. in the angular ranges of $0^\circ \leq \theta < 180^\circ$ and $180^\circ \leq \theta < 360^\circ$ in Fig. 14), while the second involves fitting a Gaussian function and taking the centre of the Gaussian as the arm location. The results of this analysis for a single time frame (0.7 Gyr in the Pert model) are shown in Fig. 15, where arms have been realigned to their true azimuth and binned into a 0.5 kpc scale. The figure shows gas and stellar arm traces, as well as the two methods of arm location. All arm features clearly trace log-spirals (appearing as straight lines in $\log(R) - \theta$ space). The bridge and tail are slightly different at this epoch, with the tail being tighter wound than the bridge arm in the stars but more unwound than the bridge in the gas. The tail also shows much greater scatter than the bridge in the gas, which is likely due to the large spurring and strong radial decay of the arm at large radii (see the 0.7 Gyr time-stamp in Fig. 6). The difference between the peak and Gaussian fitting techniques is only minor in each case, which was also concluded by Egusa et al. (2017). The dashed lines show fits to the log-spiral function. Only the fits to the peak-finding points are shown, as there was only minor difference to the Gaussian fit. The pitch angles measured for the gas arms are $\alpha = 15^\circ$ for the bridge and $\alpha = 18^\circ$ for the tail, whereas the stars are best fitted by $\alpha = 15^\circ$ for the bridge and $\alpha = 14^\circ$ for the tail.

Offsets between stellar and gaseous arms are shown in Fig. 16, simply calculated from the difference between the points in Fig. 15. Here, we show three time-stamps of the Pert simulation (0.6, 0.7 and 0.8 Gyr) and one of the noFBSF case (0.7 Gyr). The grey shaded

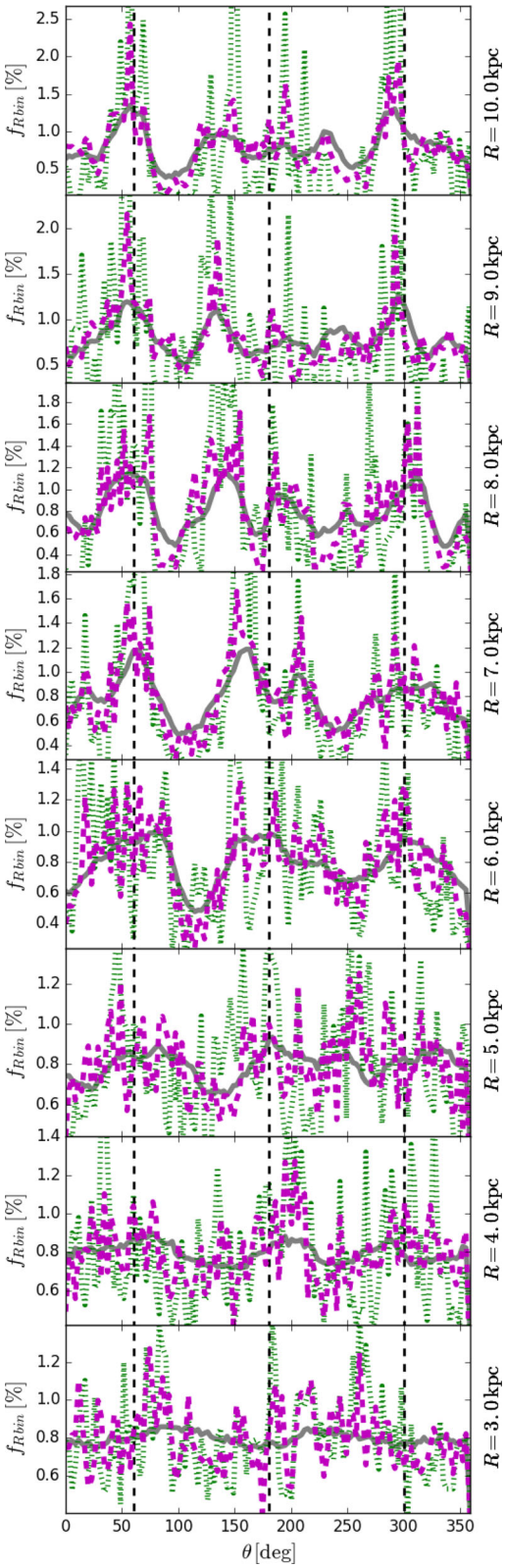

Figure 13. Location of old stellar (solid grey), gaseous (dashed magenta) and young stellar (dotted green) features in the Live galactic disc simulation and 600 Myr of evolution. The *y*-axis shows the fraction of particles as a function of azimuth that are present in the denoted annulus; f_{Rbin}. Material has been phase shifted to align to the fitted stellar spiral arms (black dashed lines).

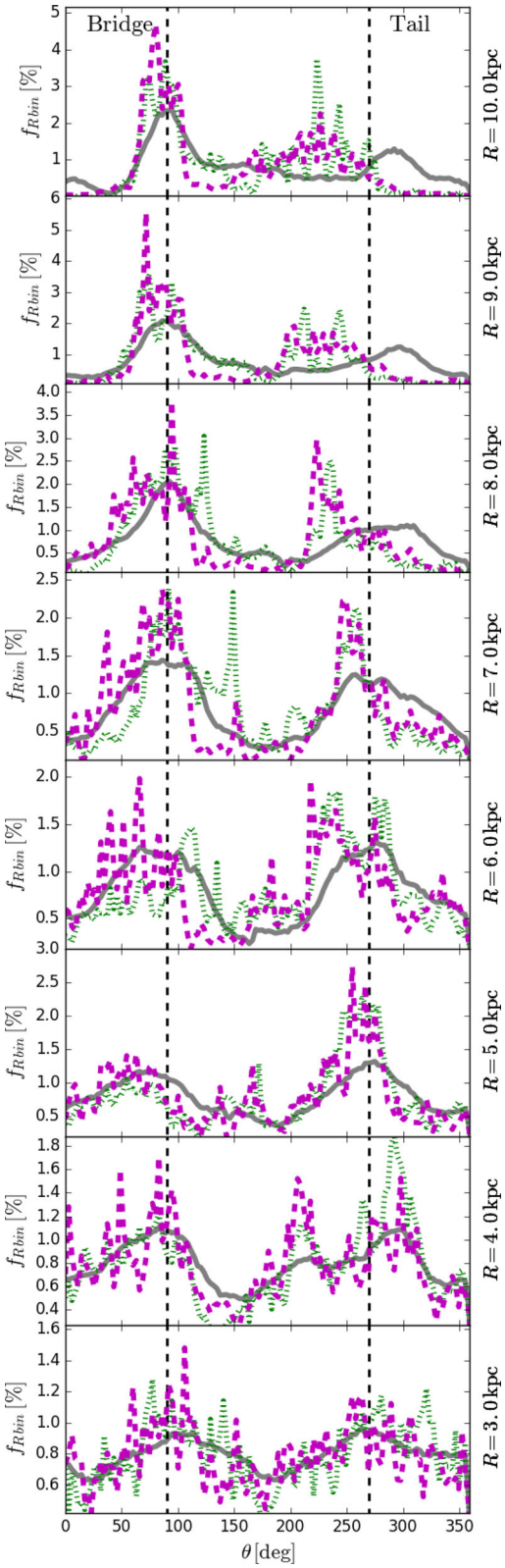

Figure 14. As Fig. 13 but for the perturbed stellar disc after 700 Myr of evolution. Note that peaks are slightly offset between the different media compared to the arms in Fig. 13. The right-hand dashed line is the tail (the large offset at 10 kpc), and the left-hand dashed line is the bridge.

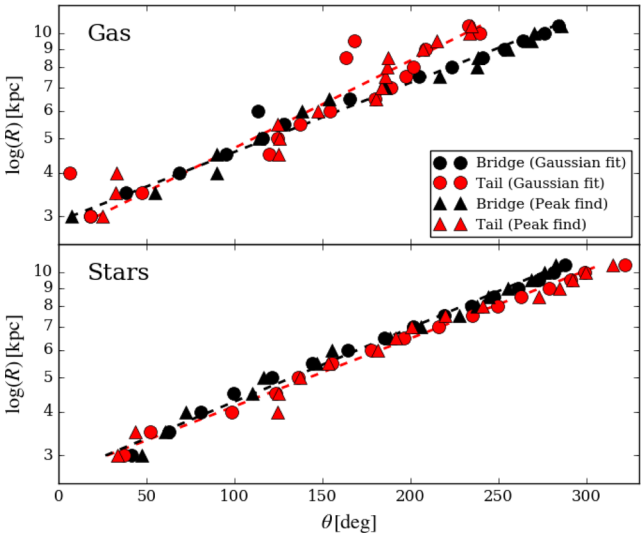

Figure 15. Tracing of the arms in the perturbed spiral simulation at 700 Myr. The top panel shows the gaseous arms and the bottom the stellar arms. Black points show the bridge arm and red points the tail arm. Triangles denote arm finding by simply picking the peak, and circles by fitting a Gaussian to arm sections. Dashed lines show log-spiral fits to the bridge and tail arms for the peak-finding method (results were similar using the Gaussian fitting so for clarity a line is not shown).

region in the 0.6 Gyr time-stamp shows where an $m = 2$ spiral could not be fit, as the spiral had not yet reached the inner disc. The earliest time frame (0.6 Gyr) shows that no strong offset between the stars and the gas is evident. There is a slight positive offset in the inner disc (where gas is on the convex side of the stellar spiral) and negative at outer radii (gas on the concave side), but the latter is only for the peak-find method. The positive offset component can be seen in Fig. 7 where the southern arm has strayed from a log-spiral in the gas pointing directly to the perturber. At 0.7 Gyr, there is a clear positive offset at almost all radii. In the inner and mid-disc this offset is in the range of 5°–25°. The extremely large offsets in the outer disc are due to the gas tail branching at around 9 kpc (seen in Figs 6, 10 and 12 at 700 Myr). The stellar arm continues to trace a log-spiral structure at this radii, whereas the gas deviates away to a much wider arm. At later times this wide branch dissipates, leaving only the shorter gas spiral that follows the stellar arm much closer. Only minor differences are seen between the different arm definitions. The noFBSF calculation shows similar features to the more sophisticated model, with a preference to positive offsets that is stronger at outer radii. In general, the offsets appear slightly weaker in this hydrodynamic+gravity-only run.

At the later time-stamp (0.8 Gyr), the offsets show a much greater scatter with radius, though still showing a general preference to gas being on the convex side of the stellar arms. The binned data also

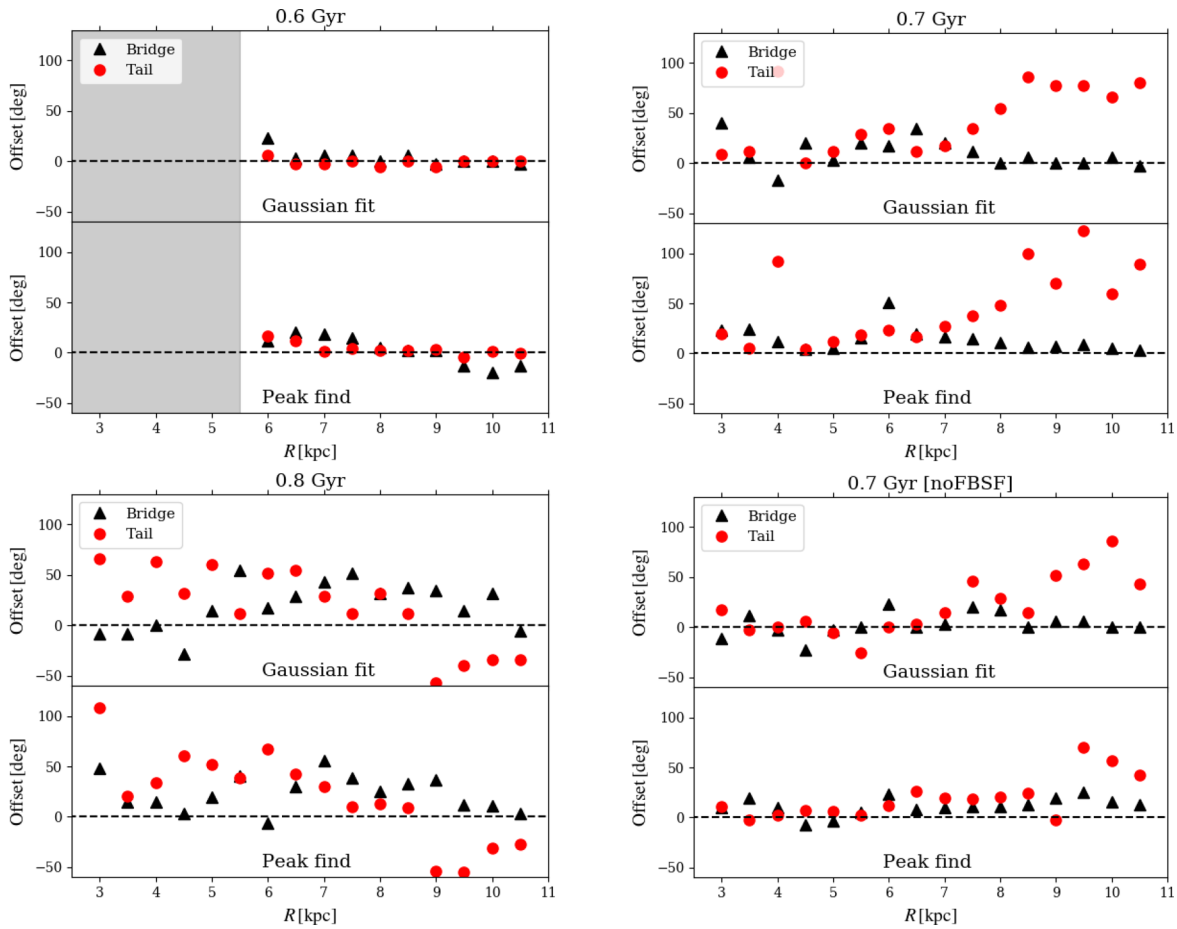

Figure 16. The offset between gaseous and stellar arms using the Gaussian fitting (top panels) and peak finding (bottom panels) methods in four different simulation time-stamps. Red circles show tail arm offsets, and black triangles the bridge arm offsets. The bottom-right plot shows the same time frame as the top right (0.7Gyr) but for a calculation without cooling, star formation and feedback. The shaded grey regions indicate radii where two-armed tidal spirals were not the dominant arm feature. Gas on the concave side of the stellar arms is defined as having negative offset (as upstream is defined in Egusa et al. 2017).

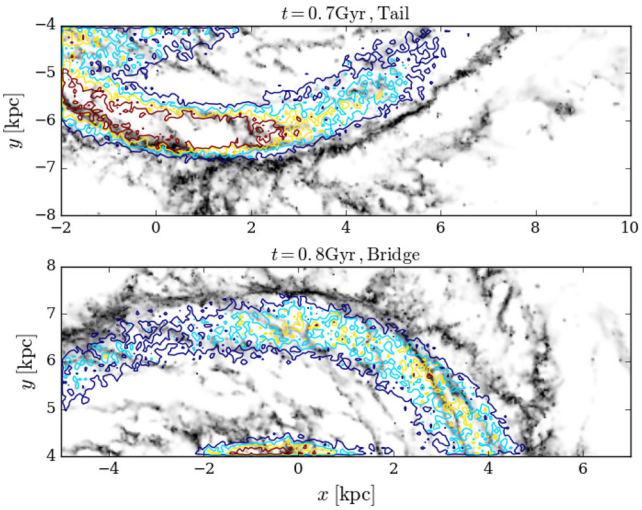

Figure 17. Two arm regions showing clear offsets in the gas (grey-scale render), and stars (coloured contours) at two different times (0.7 and 0.8 Gyr). The earlier time frame focuses on the offset in the tail, and the latter the bridge. Notice the weaker stellar surface density in the bridge arm at this time. Both images have been rotated in z-axis so that the arms lie horizontally.

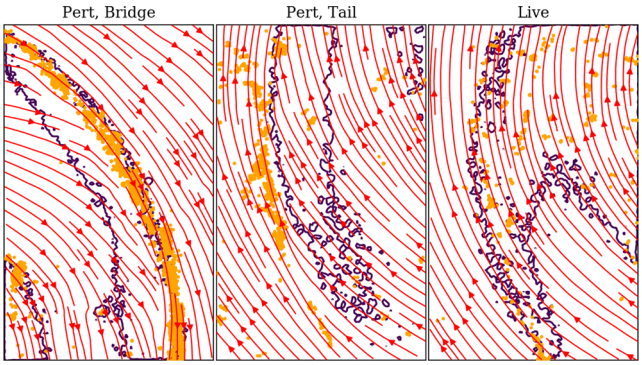

Figure 18. Plot of velocity fields around different spiral arms. From left to right: the bridge in a perturbed run, the tail in the same run and an arm in the isolated live disc. Contours show the stellar density, and the orange points the regions of star formation. The stellar density field contour for the Live data has a value half that of the perturbed run due to the weaker nature of the spiral arms. Plots have dimensions of approximately 7 kpc by 4 kpc.

highlight this (bottom panels Fig. 12), with several arm components appearing offset in the gas compared to the stars. There is a minor negative offset component in the tail arm at a large radius. Inspection of top–down maps shows that in this region the tail arm is somewhat disconnected from the mid and inner discs (also visible in Fig. 12) and is a combination of a few particularly large spurs/branches that are leaving the bridge arm and falling into the stellar potential well. This can be seen in the southern arm at 0.8 Gyr in Fig. 7 where the arm seems to be winding inwards to a couple of large spurs breaking away from the northern bridge arm.

In general, these models show the gas arms lying on the convex side of the stellar arms approximately 300 Myr after the closest approach, with each arm showing a slightly different response, particularly in the outer disc region. Fig. 17 shows just how strong these offsets appear between the two different media, with stars (contours) and gas (render) showing a visible offset in two different arms at two different locations. In Fig. 18, we show a selection of stellar spiral arms (contours) with overlaying stellar velocity streamlines, as well as the star formation front (stars with ages <20 Myr) as orange points. The first two panels show the same model as the 0.7 Gyr model of Fig. 17 but now showing both bridge and tail arms, and the far right-hand panel shows an arm from the Live model (the same time frame as Fig. 5). It can clearly be seen that the velocity field in the perturbed spiral arms has regions of orbital crowding, with streamlines indicating the gas and star formation pile-up at the outside edge of the stellar spiral arms. Streamlines transition from an oblique angle to the arms, and then parallel to the arms after passing through. The star-forming events are clustered along this pile-up zone, clearly offset from the stellar arms. The arms in the isolated stellar disc instead appear to leave the global velocity field relatively unperturbed, with no clear changes in direction after passing through the arms. The star-forming regions in this arm seem uniformly scattered around the stellar arm, with no well-defined formation front.

Comparing to other numerical studies; a similar convex-side offset is also seen by Wada (2008), and in the <6 kpc region of the feedback/star formation model of Baba et al. (2015). However, both of these models used a density wave potential, which has clear corotation regions unlike these tidal arms and should result in different shock locations and offsets with radius. The best measurements of spiral arm offsets in observations come from M51. Recently, Egusa et al. (2017) looked into offsets between stellar and gaseous arms, seeing density-wave-like offsets in the bridge arm (their 'arm2') in the inner disc, showing a positive offset of the gas arm (downstream assuming their corotation placement). They also see negative offsets in a number of locations for the tail arm (their 'arm1'), though there is a considerable scatter in their measured points. They also claim large uncertainties in outer disc data, which is where our offsets are greatest. It is, however, somewhat problematic to compare our model with M51 directly, as the orbital configuration and mass models have not been tailored to the M51 system in any way. A more consistent comparison would come of using the initial conditions of Salo & Laurikainen (2000); Dobbs et al. (2010) or Chakrabarti et al. (2011) with the physics and resolution used here.

3.3.4 Interarm spurs

Spur features have been seen in numerous simulations of spiral galaxies, and yet their origin is a topic of debate. Wada & Koda (2004) propose that these features are a result of Kelvin–Helmholtz instabilities, whereas Dobbs & Bonnell (2006) interpret these features simply as the orbit crowding of gas that is then sheared out by differential rotation (see also Kim & Ostriker 2006, Shetty & Ostriker 2006, Kim, Kim & Kim 2014). Fig. 19 shows an image of the gas in the perturbed disc with two different spur structures highlighted (panel a), one in the bridge and one in the tail. Clear spurring-like features are seen, with those of the outer arm being stronger than the inner. Spirals of M51 are shown in the insert, where spurring features are also seen. The spurs here are uneven in nature, both within in an arm and between the bridge and tail. The spurs appear much larger in the bridge (left-hand) arm, which is currently the arm with the dominant star formation activity (see Fig. 11). Some of the largest spurs even connect between the arms, for example the long branch-like features to the left of the eastern spur ($x \approx 4$ kpc, $y \approx 3$ kpc) that appears as a result of a large gas clump being between the tail arm it just left and the approaching bridge arm.

While the gas shows clear spurring features, it is worth mentioning at what form does the stellar distribution take. The old stellar

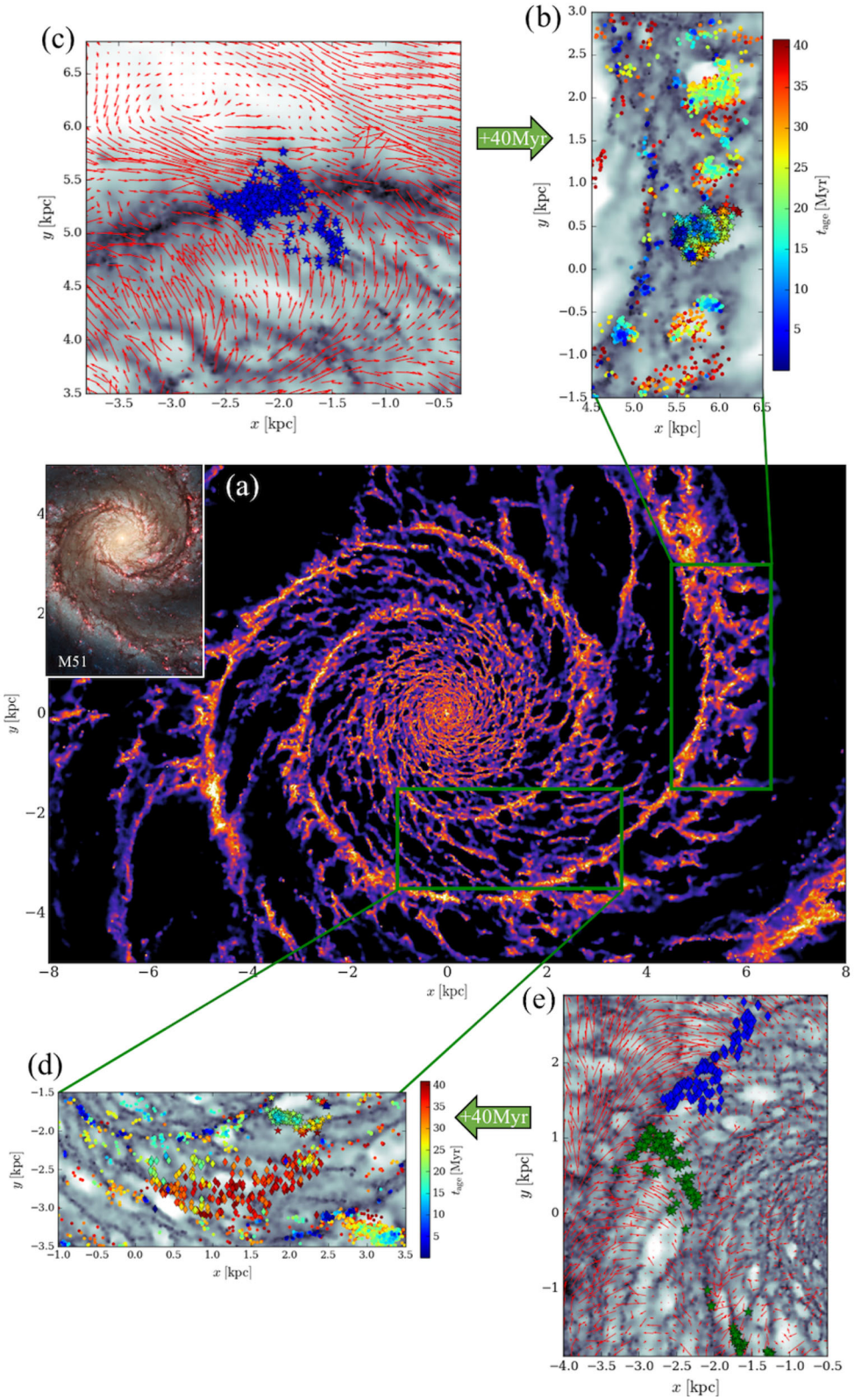

Figure 19. A focus on spurs in the perturbed galactic disc. Panel (a) shows the large-scale structure of the gas disc, with M51 shown in the insert for comparison of similar tidal spirals in nature. Panels (b) and (d) show two regions of the disc with spur-like features, where young (<40 Myr) star particles are overplotted as symbols coloured by their ages. Panels (c) and (e) show the starred and diamond regions of (b) and (d) 40 Myr earlier, prior to the birth of these young stars. In (c) and (e), the corresponding parent gas particles to the new stars, shown as diamond and starred points in (c) and (d) are shown as coloured symbols. The local gas velocity field is shown by the red vector arrows. M51 image credit: NASA, ESA, S. Beckwith (STScI) and The Hubble Heritage Team (STScI/AURA).

population is very smooth, but the young stars show a level of substructure. Panels (b) and (d) show the spurred simulation regions again, now zoomed in and showing the young stellar population as coloured points. We defined young stars here as having ages <40 Myr, and the points are coloured by their ages. In the (b) arm, the youngest (bluer) stars are seen being born on the spiral arm itself, while the intermediate-aged stars are flowing out of the spiral in clear clusters. The feedback from some of these clusters appears to be enforcing the cavities between spurs, as they appear coincident with voids in the gas. In the (d) region, the spurs are much weaker but more uniform in shape, showing segments a few kpc long. Despite some high-density gas deposits in the spur regions, the youngest stars lie almost entirely along the spiral arm trough, with the older stars occupying most of the interarm region. These types of structures are sometimes denoted 'feathers' in the literature as they have little or no star formation, whereas spurs are defined as short, high-density regions with active star formation (e.g. Renaud et al. 2013).

In panels (c) and (e), we show the parent gas particles of the young stars seen in (b) and (d), showing the structure of the gas that birthed the young stars found in the spur regions. These data are shown 40 Myr in the past of (b) and (d), far enough in the past as to be prior to the birth of the oldest 'young' star. We have only plotted a subset of the stars in (b) and (d), chosen to highlight what appear to be unique features. In (b), these are the points indicated by star symbols, which are born from the blue starred gas particles in (c). In (d), two regions were selected. One is the older interarm region (diamond symbols) with stars born from the blue diamonds in (e). The other is a short intermediate-aged spur (star symbols in the top right of d) with stars born from the green starred gas particles in (e). A grey-scale of the gas density is shown in the background, with additional red vector arrows indicating the rotation-subtracted velocity field of the gas. In both (c) and (e), the velocity field shows material entering the arms from both directions, though the gas on the outside edge of the arm is moving nearly parallel to the arm, whereas the gas on the inside is flowing in almost perpendicular to the arm. Over the 40 Myr period all three subsets of young stars seem to show a similar structure in their parent gas particles as they do after passing through the spiral. For instance, the blue diamonds in (e) show an elongated branch while the green starred points appear as a short upstream spur in gas that then transforms into a short downstream spur.

Fig. 7 shows that spur features are evident at most times after the interaction, though become increasingly difficult to identify after the 1 Gyr time-stamp due to the complex morphology and cavities bored out by the two high-density clumps. Inspection of the isolated spiral in Fig. 5 shows no clear spur features on the scale of the perturbed disc. There are some very small interarm features, but they appear to be the result of clustered supernova cavities being sheared out by rotation. This is similar to the Static disc case (Fig. 2) though, as there is no clear stellar structure, it is difficult to define quite what is meant by a spur in this model.

4 CONCLUSIONS

In this work, we have presented a study of the gas morphology and star formation process in a tidally induced spiral galaxy using simulations including cooling, star formation and stellar feedback. The tidal encounter greatly boosts the star formation activity in the disc, and causes bursts of star formation in the bridge and tail spiral arms. The two arms exhibit a temporal offset in their bursts of star formation. Activity is first being boosted in the tail arm then the bridge arm, the result of gas stripping by the companion passage delaying the star formation in the bridge and extreme orbit overlapping in the tail arm causing rapid gas compression.

The gaseous arms appear offset azimuthally compared to stellar arms, an effect not seen in the dynamic arms seen pre-interaction. These offsets are different between each arm, and appear to be highly time dependent. They do, however, show a clear preference for gas arms to be on the convex side of the stellar spiral potential well. Finally, we also observe spurring features in the interarm regions, similar to those seen in density wave spiral simulations and observations. Inner spurs appear the result of purely shearing motion in high-density gas in the arms, whereas the presence of outer spurs is exemplified by clustered feedback by newly formed stars leaving the spiral arm.

These findings further separate tidal spirals from the other spiral generation mechanisms in the literature; providing valuable diagnostics for observations of the ISM in external galaxies. With the resolution of current surveys, such diagnostics are out of reach for all but the nearest spiral galaxies. Yet they will become increasingly important as we move closer towards pc scale observations and in turn a unified theory of spiral structure.

ACKNOWLEDGEMENTS

We thankthe referee, Curtis Struck, for his reading of this manuscript and insightful comments/suggestions that have improved this work. Numerical computations were (in part) carried out on Cray XC30 at Center for Computational Astrophysics, National Astronomical Observatory of Japan and the GPC supercomputer at the SciNet HPC Consortium (Loken et al. 2010). SciNet is funded by: the Canada Foundation for Innovation under the auspices of Compute Canada; the Government of Ontario; Ontario Research Fund – Research Excellence; and the University of Toronto. SMB acknowledges support from the Vanier Canada Graduate Scholarship Program. We used the PYNBODY (Pontzen et al. 2013) and YT (Turk et al. 2011) packages for parts of our analysis and plotting of data. We thank T. Okamoto and T. Saitoh for helpful discussions on this work.

REFERENCES

Agertz O., Teyssier R., Moore B., 2009, MNRAS, 397, L64
Agertz O., Kravtsov A. V., Leitner S. N., Gnedin N. Y., 2013, ApJ, 770, 25
Agertz O., Romeo A. B., Grisdale K., 2015, MNRAS, 449, 2156
Athanassoula E., 1992, MNRAS, 259, 345
Baba J., Morokuma-Matsui K., Egusa F., 2015, PASJ, 67, L4
Baba J., Morokuma-Matsui K., Miyamoto Y., Egusa F., Kuno N., 2016, MNRAS, 460, 2472
Benincasa S. M., Wadsley J., Couchman H. M. P., Keller B. W., 2016, MNRAS, 462, 3053
Bertin G., Lin C. C., Lowe S. A., Thurstans R. P., 1989, ApJ, 338, 78
Bigiel F., Leroy A., Walter F., Brinks E., de Blok W. J. G., Madore B., Thornley M. D., 2008, AJ, 136, 2846
Binney J., Merrifield M., 1998, Galactic Astronomy. Princeton Univ. Press, Princeton, NJ
Binney J., Tremaine S., 1987, Galactic Dynamics. Princeton Univ. Press, Princeton, NJ
Boily C. M., Kroupa P., Peñarrubia-Garrido J., 2001, New Astron., 6, 27
Bottema R., 2003, MNRAS, 344, 358
Chakrabarti S., Bigiel F., Chang P., Blitz L., 2011, ApJ, 743, 35
Contopoulos G., Papayannopoulos T., 1980, A&A, 92, 33
D'Onghia E., 2015, ApJ, 808, L8
Di Matteo P., Combes F., Melchior A.-L., Semelin B., 2007, A&A, 468, 61

Di Matteo P., Bournaud F., Martig M., Combes F., Melchior A.-L., Semelin B., 2008, A&A, 492, 31
Dobbs C., Baba J., 2014, PASA, 31, 35
Dobbs C. L., Bonnell I. A., 2006, MNRAS, 367, 873
Dobbs C. L., Pringle J. E., 2010, MNRAS, 409, 396
Dobbs C. L., Theis C., Pringle J. E., Bate M. R., 2010, MNRAS, 403, 625
Dobbs C. L., Burkert A., Pringle J. E., 2011, MNRAS, 417, 1318
Dobbs C. L., Pringle J. E., Burkert A., 2012, MNRAS, 425, 2157
Donner K. J., Engstrom S., Sundelius B., 1991, A&A, 252, 571
Dubinski J., Chakrabarty D., 2009, ApJ, 703, 2068
Egusa F., Mentuch Cooper E., Koda J., Baba J., 2017, MNRAS, 465, 460
Elmegreen B. G., Thomasson M., 1993, A&A, 272, 37
Elmegreen D. M., Sundin M., Sundelius B., Elmegreen B., 1991, A&A, 244, 52
Elmegreen B. G. et al., 2000, AJ, 120, 630
Few C. G., Dobbs C., Pettitt A., Konstandin L., 2016, MNRAS, 460, 4382
Fujimoto M., 1968, in Arakelyan A., ed., Proc. IAU Symp. 29, Non-stable Phenomena in Galaxies. The Publishing House of the Academy of Sciences of Armenian SSR Yerevan p. 453 [translated from Russian]
Fujimoto Y., Bryan G. L., Tasker E. J., Habe A., Simpson C. M., 2016, MNRAS, 461, 1684
Gabor J. M., Capelo P. R., Volonteri M., Bournaud F., Bellovary J., Governato F., Quinn T., 2016, A&A, 592, A62
Gittins D. M., Clarke C. J., 2004, MNRAS, 349, 909
Goldbaum N. J., Krumholz M. R., Forbes J. C., 2016, ApJ, 827, 28
Governato F., Willman B., Mayer L., Brooks A., Stinson G., Valenzuela O., Wadsley J., Quinn T., 2007, MNRAS, 374, 1479
Grand R. J. J., Kawata D., Cropper M., 2012, MNRAS, 426, 167
Grisdale K., Agertz O., Romeo A. B., Renaud F., Read J. I., 2017, MNRAS, 466, 1093
Hayward C. C., Torrey P., Springel V., Hernquist L., Vogelsberger M., 2014, MNRAS, 442, 1992
Hopkins P. F., Quataert E., Murray N., 2012, MNRAS, 421, 3488
Hopkins P. F., Cox T. J., Hernquist L., Narayanan D., Hayward C. C., Murray N., 2013a, MNRAS, 430, 1901
Hopkins P. F., Narayanan D., Murray N., 2013b, MNRAS, 432, 2647
Hopkins P. F., Kereš D., Oñorbe J., Faucher-Giguère C.-A., Quataert E., Murray N., Bullock J. S., 2014, MNRAS, 445, 581
Kalnajs A. J., 1973, PASA, 2, 174
Katz N., 1992, ApJ, 391, 502
Katz N., Weinberg D. H., Hernquist L., 1996, ApJS, 105, 19
Kaufman M., Elmegreen B. G., Struck C., Elmegreen D. M., Bournaud F., Brinks E., Juneau S., Sheth K., 2016, ApJ, 831, 161
Keller B. W., Wadsley J., Benincasa S. M., Couchman H. M. P., 2014, MNRAS, 442, 3013
Keller B. W., Wadsley J., Couchman H. M. P., 2015, MNRAS, 453, 3499
Kendall S., Kennicutt R. C., Clarke C., 2011, MNRAS, 414, 538
Kennicutt R. C. jr., 1998, ApJ, 498, 541
Khoperskov A. V., Eremin M. A., Khoperskov S. A., Butenko M. A., Morozov A. G., 2012, Astron. Rep., 56, 16
Kim W.-T., Ostriker E. C., 2006, ApJ, 646, 213
Kim W.-T., Kim Y., Kim J.-G., 2014, ApJ, 789, 68
Lin C. C., Shu F. H., 1964, ApJ, 140, 646
Loken C. et al., 2010, J. Phys. Conf. Ser., 256, 012026
Mayer L., Tamburello V., Lupi A., Keller B., Wadsley J., Madau P., 2016, ApJ, 830, L13
Meidt S. E., Rand R. J., Merrifield M. R., Shetty R., Vogel S. N., 2008, ApJ, 688, 224
Moreno J., Torrey P., Ellison S. L., Patton D. R., Bluck A. F. L., Bansal G., Hernquist L., 2015, MNRAS, 448, 1107
Oh S. H., Kim W.-T., Lee H. M., Kim J., 2008, ApJ, 683, 94
Oh S. H., Kim W.-T., Lee H. M., 2015, ApJ, 807, 73
Okamoto T., Eke V. R., Frenk C. S., Jenkins A., 2005, MNRAS, 363, 1299
Pettitt A. R., Dobbs C. L., Acreman D. M., Bate M. R., 2015, MNRAS, 449, 3911
Pettitt A. R., Tasker E. J., Wadsley J. W., 2016, MNRAS, 458, 3990 (Paper 1)
Pontzen A., Roškar R., Stinson G., Woods R., 2013, Astrophysics Source Code Library, ascl:1305.002
Renaud F. et al., 2013, MNRAS, 436, 1836
Roberts W. W., 1969, ApJ, 158, 123
Rosdahl J., Schaye J., Dubois Y., Kimm T., Teyssier R., 2017, MNRAS, 466, 11
Saitoh T. R., Daisaka H., Kokubo E., Makino J., Okamoto T., Tomisaka K., Wada K., Yoshida N., 2008, PASJ, 60, 667
Saitoh T. R., Daisaka H., Kokubo E., Makino J., Okamoto T., Tomisaka K., Wada K., Yoshida N., 2009, PASJ, 61, 481
Salo H., Laurikainen E., 2000, MNRAS, 319, 377
Schinnerer E. et al., 2013, ApJ, 779, 42
Schmidt M., 1959, ApJ, 129, 243
Sellwood J. A., 2011, MNRAS, 410, 1637
Sellwood J. A., Carlberg R. G., 1984, ApJ, 282, 61
Shen S., Wadsley J., Stinson G., 2010, MNRAS, 407, 1581
Shetty R., Ostriker E. C., 2006, ApJ, 647, 997
Stadel J. G., 2001, PhD thesis, Univ. Washington
Stinson G., Seth A., Katz N., Wadsley J., Governato F., Quinn T., 2006, MNRAS, 373, 1074
Struck C., 1997, ApJS, 113, 269
Struck C., Dobbs C. L., Hwang J.-S., 2011, MNRAS, 414, 2498
Tacconi L. J., Young J. S., 1986, ApJ, 308, 600
Tasker E. J., Bryan G. L., 2006, ApJ, 641, 878
Tasker E. J., Bryan G. L., 2008, ApJ, 673, 810
Tasker E. J., Tan J. C., 2009, ApJ, 700, 358
Tasker E. J., Wadsley J., Pudritz R., 2015, ApJ, 801, 33
Toomre A., 1981, in Fall S. M., Lynden-Bell D., eds, Structure and Evolution of Normal Galaxies. Cambridge Univ. Press, Cambridge, p. 111
Toomre A., Toomre J., 1972, ApJ, 178, 623
Turk M. J., Smith B. D., Oishi J. S., Skory S., Skillman S. W., Abel T., Norman M. L., 2011, ApJS, 192, 9
Wada K., 2008, ApJ, 675, 188
Wada K., Koda J., 2004, MNRAS, 349, 270
Wada K., Baba J., Saitoh T. R., 2011, ApJ, 735, 1
Wadsley J. W., Stadel J., Quinn T., 2004, New Astron., 9, 137
Wallin J. F., Stuart B. V., 1992, ApJ, 399, 29
Ward R. L., Benincasa S. M., Wadsley J., Sills A., Couchman H. M. P., 2016, MNRAS, 455, 920
Wolfire M. G., McKee C. F., Hollenbach D., Tielens A. G. G. M., 2003, ApJ, 587, 278

This paper has been typeset from a TEX/LATEX file prepared by the author.